SCIENCE CHINA
Technological Sciences

•Article•

March 2023 Vol.66 No.3: 706–720
https://doi.org/10.1007/s11431-022-2271-8

Improved analytical model for mesh stiffness calculation of cracked helical gear considering interactions between neighboring teeth

NING JieYu, CHEN ZaiGang* & ZHAI WanMing

State Key Laboratory of Traction Power, Southwest Jiaotong University, Chengdu 610031, China

Received September 3, 2022; accepted November 25, 2022; published online February 15, 2023

As one of the most typical fault forms of the helical gear, the crack will change the dynamic excitation and further affect the dynamic behaviors of the transmission systems. Due to the complicated structure of the helical gears, the coupling effect between the neighboring loaded teeth is usually ignored in the mesh stiffness calculation, making it considerably overestimated especially in the case of the crack fault. An improved mesh stiffness calculation method of helical gear with spatial crack is proposed to make up this gap. The interactions between the loaded neighboring teeth induced by the gear body flexibility were considered to improve the calculation accuracy and applicability. Besides, the load distribution law for the engaged cracked tooth along the tooth width and profile can be obtained. The results indicated that the mesh stiffness of the multi-tooth engagement calculation using this model could be further improved compared with the traditional methods. Finally, the effects of the helix angle, crack depth, and crack propagation length on the mesh stiffness and load distribution were investigated using the proposed method.

mesh stiffness, helical gear, structural coupling effect, slice method, spatial crack

Citation: Ning J Y, Chen Z G, Zhai W M. Improved analytical model for mesh stiffness calculation of cracked helical gear considering interactions between neighboring teeth. Sci China Tech Sci, 2023, 66: 706–720, https://doi.org/10.1007/s11431-022-2271-8

1 Introduction

The helical gear tooth load in the alternate engagement region is gradually loaded and unloaded. Therefore, the helical gear transmission is suitable for complicated high-speed and heavy-haul mechanical equipment to deliver force and motion. In addition, the impact, vibration, and noise are low for the transmission systems during the operation process. However, the fault will inevitably occur due to the complex internal excitations and external vibration environments [1,2]. As a typical fault of the helical gear, the crack presenting the complicated spatial propagation can significantly reduce the effective load-bearing region for both the tooth and gear body. Therefore, accurately obtaining the time-varying mesh stiffness of helical gear pairs with the complicated spatial crack propagation path is the premise of the relevant dynamic analysis and crack fault diagnosis.

Actually, an increasing number of scholars are performing studies on calculating of the mesh stiffness of the gear pair with crack fault from the perspective of the crack fault effect on the tooth part. Lewicki and Ballarini [3] performed analytical and experimental studies to investigate the propagation paths of the tooth root crack with different backup ratios which determined the crack path propagating to the tooth part or gear body. Verma et al. [4] researched the tooth root crack propagation effect on the mesh stiffness under different backup ratios by adopting the extended finite element (FM) method. Wang et al. [5] employed the analytical FM method to calculate the mesh stiffness of the gear pair with gear body crack and complex gear body foundation, such as thin-web and holes foundation. Based on ref. [5], the FM theory and loaded tooth analysis, Chen et al. [6] further took the situations of the slots foundation and tooth root cracks into account. Raghuwanshi and Parey [7] adopted the strain gauge

*Corresponding author (email: zgchen@swjtu.edu.cn)

technique to measure the mesh stiffness of the spur gear pair with the tooth root crack. Patel and Shakya [8] calculated the time-varying mesh stiffness of the cracked gear pair based on the potential principle, which was incorporated into a lumped parameter dynamics model of the gear pairs to perform the fault diagnosis of the tooth root crack using variational mode decomposition. Chen and Shao [9] proposed the mesh stiffness calculation method for the non-uniform tooth root crack based on the slice method, and established the corresponding relationship between the dynamic responses of the gear system and crack propagation. Furtherly, they determined the relationship between the tooth errors and the comprehensive mesh stiffness, and investigated the effects of the tooth profile modification and tooth root crack on the engagement features [10]. Mohammed et al. [11] established the time-varying mesh stiffness calculation method and the corresponding dynamics model of the gear pair with tooth root crack, and evaluated the crack propagation effect on the dynamic behaviors with several statistical indicators. Wan et al. [12] researched the dynamic behaviors of the gear-rotor system where the mesh stiffness considered the flexibility between the root circle and the base circle. Ma et al. [13] improved the mesh stiffness calculation method for the gear pair considering the transition curve equation to receive better calculation accuracy. In addition, the effects of the extended tooth contact [14] and crack propagation paths [15] on the fault characteristics of the gear systems were investigated. Pandya and Parey [16,17] studied the effects of different crack parameters and paths on the mesh stiffness of the spur gear for both low and high contact ratios. Yu et al. [18] researched the spatial propagation effect of the tooth root crack on the mesh stiffness and the load sharing factor. Cui et al. [19] presented a universal tooth profile equation according to the actual manufacturing to improve the mesh stiffness for the cracked tooth. Meng et al. [20] calculated the mesh stiffness of the cracked gear pair and analyzed the vibration characteristics of the gear systems. Jiang and Liu [21] modeled the dynamics model of the cracked helical gear pair considering the axial stiffness components and the gear body deflections. Tang et al. [22] developed two coupling models to calculate the mesh stiffness of the helical gears. Huangfu et al. [23] established more detailed spalling geometries and analyzed the contact features and dynamic behaviors of the gear systems from the theoretical and experimental study perspectives, and then the effect of the tip relief was further investigated under the wear fault [24].

All the above literature only considered the crack fault effect on the tooth stiffness component and that on the gear body-induced stiffness component was ignored. Based on the aforementioned research, some scholars performed their scientific research from the perspective of the effect of the crack fault on the gear body part for the spur gear. Actually, the effective load-bearing region on the gear body would be reduced when there is the presence of a crack fault. Considering the actual bearing zone of the gear body under the crack fault, Chen et al. [25] performed the geometric modification of the effective load-bearing region and center of the gear body under the condition that the presence of the tooth root crack and the improved calculation method was employed into the locomotive system with tooth root crack for dynamic features analysis [26,27]. Ning et al. [28] established the mapping relationship between the vibration responses of the support bearings and the crack propagation of the gear system. Yang et al. [29] improved the cantilever beam model of the gear with tooth root crack, which was applicable to situations where the crack propagated in both the tooth part and the gear body. They further studied the effect of the different crack opening states on the mesh stiffness and the dynamic characteristics of the gear systems [30]. Wang and Zhu [31] calculated the mesh stiffness variations of the gear pair under the different spatial crack propagations with the modified method.

The gear body-induced stiffness was simply superimposed in the multi-tooth engagement in the above literature. Therefore, the total gear body-induced stiffness would be overestimated in the multi-tooth engagement as the engaged tooth pairs share one gear body, eventually overestimating the comprehensive mesh stiffness for the double-tooth engagement region. Feng et al. [32] introduced the modified coefficients of the fillet-foundation stiffness in the mesh stiffness calculation, and the coefficients could be determined by ref. [33] via the finite element model to solve the above problem and obtain a more accurate mesh stiffness for the dynamic analysis. Then, Huangfu et al. [34] employed the modified mesh stiffness to analyze the spatial crack propagation effect of the helical gear on the mesh stiffness. Xie et al. [35] deduced the analytical formulas for the gear body-induced deflection when the neighboring tooth was loaded to theoretically reveal the coupling effect between the two neighboring teeth in the double-tooth region for the healthy spur gear. Then, it was introduced into the mesh stiffness calculation [36,37] and analysis of the nonlinear dynamic behaviors [38] for the spur system.

The effective load-bearing region reduction of the gear body would be reflected in the geometric parameters of the gear body, and more than that, it can vary the coefficients of the polynomial formulas employed to calculate the gear body-induced stiffness. In addition, the structural coupling effect between the neighboring teeth with the crack fault in the double-tooth region is usually ignored by many researchers due to the absence of an effective method. To fill up the gap, Chen et al. [39] calculated the stiffness of the gear fillet-foundation and the structural coupling effect with the tooth root crack via the finite element method. However, the mesh stiffness calculated by the finite element method was time-consuming. Ning et al. [40], considering the coupling

effect of the deformations between the neighboring teeth based on the elastic mechanics, derived the analytical formulas of the gear body-induced stiffness with the tooth root crack to obtain an efficient and accurate analytical method to calculate the gear body-induced stiffness.

As mentioned in the foregoing literature, the coupling effect between the adjacent loaded teeth induced by the gear body flexibility was only considered in the spur gear. While the coupling effect of the elastic deformation between the neighboring teeth is usually ignored in the mesh stiffness calculation for the healthy helical gears, let alone the situation for the cracked helical gear. Actually, the coupling effect between the loaded neighboring teeth has been demonstrated to have a considerable influence on the mesh stiffness of the spur gear. The theoretical calculation result will greatly deviate from the actual one in the mesh stiffness calculation of the helical gear if the structural coupling effect is ignored. Therefore, the structural coupling effect was considered in this study to calculate the mesh stiffness of the helical gear with the complex spatial crack propagation.

2 Improved mesh stiffness calculation method for the cracked helical gear

In the multi-tooth engagement of the helical gears, the loaded tooth will influence the deformation of the neighboring tooth due to that the two neighboring teeth share one gear body. Based on the analytical calculation method, the coupling effect between the neighboring teeth is introduced into the mesh stiffness calculation of the helical gear in this paper, especially for the occurrence of the spatial crack fault.

When the mating helical gears are engaging, the meshing first occurs at one end, gradually transits to the other end and finally exits engagement. The length of the contact line on the tooth surface first presents the trend of gradual growth, followed by the modest decline until nil. Due to the time-varying characteristics of the length of the contact line, the "slice method" is usually adopted in the time-varying mesh stiffness calculation for the helical gears. The schematic of the sliced helical gear model is shown in Figure 1.

According to the refs. [41,42], the actual crack of the helical gear does not only occur in the dedendum region, but shows the spatial propagation instead. The crack propagation paths of the helical gear are displayed in Figure 2, there are two types of spatial crack propagation, namely the end face propagation and the addendum propagation.

2.1 Modeling of the spatial crack propagation

The addendum propagation and end face propagation of the tooth crack are the common propagation paths in helical gear systems. In addition, there are two degrees of crack propa-

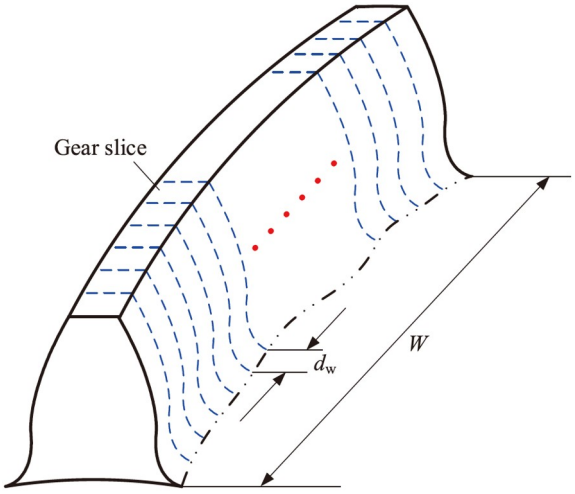

Figure 1 (Color online) Schematic of the sliced helical gear model.

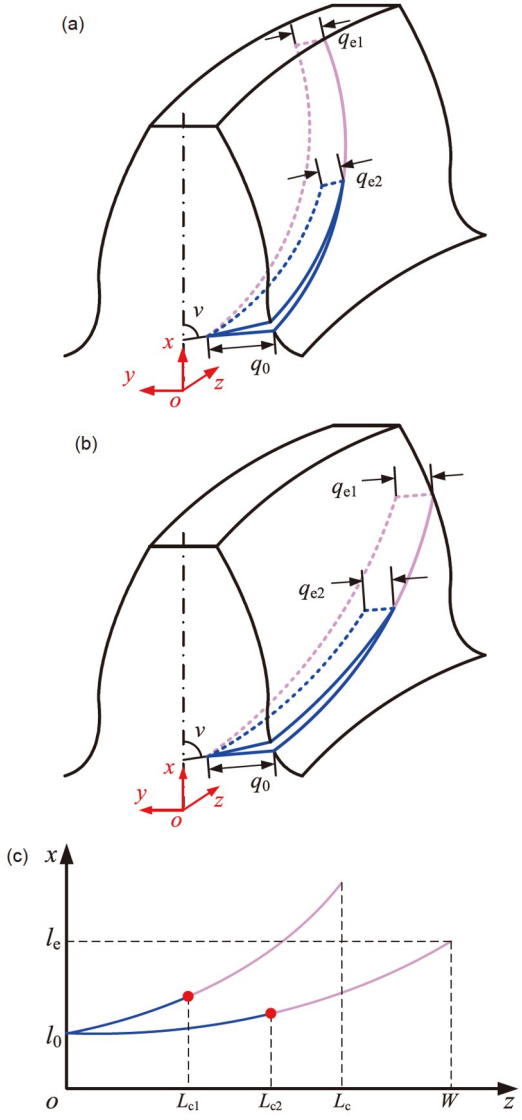

Figure 2 (Color online) Schematic of the crack propagation of the helical gear. (a) Addendum propagation; (b) end face propagation; (c) propagation paths.

gation, namely penetration and non-penetration. Therefore, the four types of the spatial crack propagation distribution on the helical gear are analyzed in this paper, namely non-penetrative addendum crack (Type-1), penetrative addendum crack (Type-2), non-penetrative end face crack (Type-3), and penetrative end face crack (Type-4). The crack propagation path is assumed to be curvilinear distribution according to the actual failure mode of the helical gear. The crack depth is modeled as the parabolic distribution.

The crack propagation paths under the four types of time-varying crack parameters are depicted in Figure 2. v is the intersection angle between the extension line of the crack and the centerline of the gear tooth. It is worth noting that the intersection angle of the crack along the propagation path is deemed as constant value in this study. q_0 is the initial crack depth of the transverse, q_1 and q_2 are the ending crack depth for penetrative and non-penetrative crack, respectively. l_0 is the distance between the dedendum circle and the initial position of the crack, l_e is the distance between the dedendum circle and the ending position of the crack for the Type-4. L_c is the width of the crack propagation. The crack depth of the different gear slice can be calculated by refs. [31,34]:

$$q_w(z)=\begin{cases} q_0\sqrt{\dfrac{L_c-z}{L_c}}\,(z\leqslant L_c)+0(z>L_c), \\ \qquad\qquad \text{non-penetrative crack}, \\ \sqrt{q_0^2-\dfrac{q_0^2-q_e^2}{L_c}z}\,, \text{ penetrative crack}, \end{cases} \tag{1}$$

where z is the coordinate in z-axis of the gear slice.

The x-axis coordinate of the crack propagation path for the gear slice can be calculated by refs. [31,34]:

$$l_w(z)=\begin{cases} l_0+\left(R_{ap}-R_{fp}-l_0\right)\left(\dfrac{z}{L_c}\right)^2, \\ \qquad\qquad \text{non-penetrative crack}, \\ l_0+\left(l_e-l_0\right)\left(\dfrac{z}{L_c}\right)^2, \text{ penetrative crack}, \end{cases} \tag{2}$$

where R_{ap} and R_{fp} denote the radius of the addendum and dedendum circle, respectively.

2.2 Stiffness components calculation with the spatial crack propagation

The tooth stiffness of the helical gear slice can be regarded as a spur gear, and the cantilever beam model with variable section of each helical gear slice is shown in Figure 3(a). Due to the presence of the helix angle, the force acting on the tooth profile of the helical gear slice can be divided into two parts, namely the transverse force acting on the *xoy* plane and the axial force acting along the z-axis, and the schematic of the axial force is depicted in Figure 3(b). According to the deformation theory of the beam, the transverse force acting on the *xoy* plane will generate the bending, shear and axial compressive deformations, and the axial force acting along the z-axis will cause the bending deformation on the *xoz* and *yoz* planes. It is worth noting that the coupling effect between the adjacent helical gear slices is of secondary importance when the influence factors affecting the contact region along the tooth width are ignored, such as tooth modification and assembling error [43]. Therefore, the interactions between the helical gear slices are not taken into account since these influencing factors are not considered in the present study.

The transverse force F_{xy} consists of the F_y along the direction of the tooth thickness and the F_x perpendicular to the tooth thickness, axial force F_z along the z-axis, they can be calculated by the mesh force F_m [44]:

$$\begin{cases} F_x=F_m\cos\beta_b\sin\alpha_m, \\ F_y=F_m\cos\beta_b\cos\alpha_m, \\ F_z=F_m\sin\beta_b, \end{cases} \tag{3}$$

where β_b is the helix angle of the base circle; α_m denotes the transverse pressure angle.

The torque M_{xy} is caused by the transverse force F_{xy}, and the torques M_{xz} and M_{yz} are induced by the axial force F_z. All three torques can be given as

$$\begin{cases} M_{xy}=x_F F_y-hF_x, \\ M_{xz}=x_F F_z, \\ M_{yz}=hF_z, \end{cases} \tag{4}$$

where x_F is the distance between the micro-section and the engaged point; h denotes the half of the tooth thickness at the

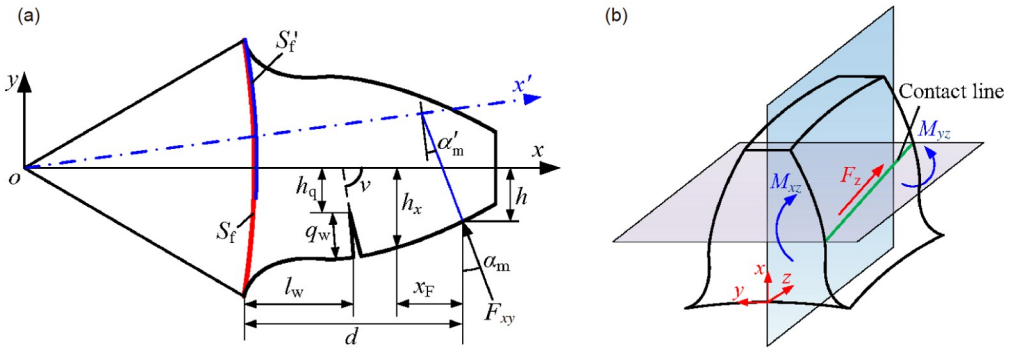

Figure 3 (Color online) Schematic of the mesh force for the helical gear. (a) End face; (b) axial direction.

point of engagement.

According to the principle of potential energy, the stored potential energy of the deformation components induced by the transverse force can be expressed as

$$\begin{cases} U_{bz}=\int_0^d \dfrac{M_{xy}^2}{2EI_{xy}}\mathrm{d}x, \\ U_s=\int_0^d \dfrac{1.2F_y^2}{2GA_x}\mathrm{d}x, \\ U_a=\int_0^d \dfrac{F_x^2}{2EA_x}\mathrm{d}x. \end{cases} \tag{5}$$

The deformation components induced by the axial force can be expressed as

$$\begin{cases} U_{bx}=\int_0^d \dfrac{M_{yz}^2}{2EI_{yz}}\mathrm{d}x, \\ U_{by}=\int_0^d \dfrac{M_{xz}^2}{2EI_{xz}}\mathrm{d}x, \end{cases} \tag{6}$$

where E and G are the Young's modulus and shear modulus, respectively; d is the effective length of the cantilever beam and the mesh force; A and I are respectively the section area and moment of inertia of the gear slice, which can be calculated by ref. [44]:

$$A_x=\begin{cases} 2h_x d_w, & h_x \leqslant h_q, \\ (h_x+h_q)d_w, & h_x > h_q, \end{cases} \tag{7}$$

$$I_{xy}=\begin{cases} \dfrac{2}{3}h_x^3 d_w, & h_x \leqslant h_q, \\ \dfrac{1}{12}(h_x+h_q)^3 d_w, & h_x > h_q, \end{cases}$$

$$I_{xz}=\begin{cases} \dfrac{1}{6}h_x d_w^3, & h_x \leqslant h_q, \\ \dfrac{1}{12}(h_x+h_q)d_w^3, & h_x > h_q \end{cases} \tag{8}$$

$$I_{yz}=I_{xy}+I_{xz},$$

where d_w is the width of the gear slice; h_x denotes half of the length for the micro-section; h_q represents the distance between the center line and the crack tip along the y-axis.

Combining the eqs. (3)–(8), the stiffness components of the total mesh stiffness can be obtained.

The bending stiffness induced by the transverse force and axial force can be respectively calculated by

$$\frac{1}{K_{bz}}=\int_0^d \frac{(x_F\cos\alpha_m - h\sin\alpha_m)^2\cos^2\beta_b}{EI_{xy}}\mathrm{d}x, \tag{9}$$

$$\begin{cases} \dfrac{1}{K_{bx}}=\int_0^d \dfrac{h^2\sin^2\beta_b}{EI_{yz}}\mathrm{d}x, \\ \dfrac{1}{K_{by}}=\int_0^d \dfrac{x_F^2\sin^2\beta_b}{EI_{xz}}\mathrm{d}x. \end{cases} \tag{10}$$

The shear stiffness and the axial compressive stiffness can be calculated by refs. [9,10]:

$$\frac{1}{K_s}=\int_0^d \frac{1.2\cos^2\alpha_m\cos^2\beta_b}{GA_x}\mathrm{d}x, \tag{11}$$

$$\frac{1}{K_a}=\int_0^d \frac{\sin^2\alpha_m\cos^2\beta_b}{EA_x}\mathrm{d}x, \tag{12}$$

where dx is the distance between the micro-section and the point of the engagement.

When the two teeth engage, elastic deformation would be formed in the contact region. The component of Hertz contact stiffness can be calculated by the simplified formula [37]:

$$\frac{1}{K_h}=\frac{4(1-\upsilon^2)}{\pi E d_w}, \tag{13}$$

where υ is the Possion's ratio.

The tooth stiffness of the single tooth for each helical gear slice can be calculated by

$$\frac{1}{K_t}=\frac{1}{K_{bx}}+\frac{1}{K_{by}}+\frac{1}{K_{bz}}+\frac{1}{K_s}+\frac{1}{K_a}. \tag{14}$$

Besides the tooth deformation, the elastic deformation of the gear body also exerts a considerable effect on the mesh stiffness when the tooth is loaded. Sainsot et al. [45] derived the analytical formulas of the gear body-induced stiffness for the healthy gear based on the assumption of the linear distributed normal stress and the constant distributed tangential stress. Furtherly, Xie et al. [35] improved the calculation formulas considering the cubic distributed normal stress and parabolic distributed tangential stress. The load-bearing region effect of the healthy tooth and cracked tooth are S_f and S_f', respectively, which are shown in Figure 3(a). Considering the variation of the load-bearing region when the crack fault occurs, Ning et al. [40] proposed analytical formulas for calculating the gear body-induced stiffness with the presence of the crack fault. The calculation equation of the gear body-induced stiffness for the healthy tooth and cracked tooth of the helical gear slice can be expressed as [35,40]

$$\frac{1}{K_f}=\begin{cases} \dfrac{\cos^2\alpha_m}{Ed_w}\left[L_f\left(\dfrac{u_f}{S_f}\right)^2+M_f\left(\dfrac{u_f}{S_f}\right)+P_f\left(1+Q_f\tan^2\alpha_m\right)\right], \\ \qquad\qquad \text{for healthy tooth}, \\ \dfrac{\cos^2\alpha_m'}{Ed_w}\left[L_{fc}\left(\dfrac{u_f'}{S_f'}\right)^2+M_{fc}\left(\dfrac{u_f'}{S_f'}\right)+P_{fc}\left(1+Q_{fc}\tan^2\alpha_m'\right)\right], \\ \qquad\qquad \text{for cracked tooth}, \end{cases} \tag{15}$$

where u_f and u_f' denote the distance between the dedendum and the point which is the intersection point between the center-line of the tooth and the line of action; α_m' is the mesh angle with geometric correction, whose detailed calculation can refer to ref. [25]. The details for determination of the L_f,

M_f, P_f, and Q_f for the healthy tooth can refer to ref. [35] and that of the L_{fc}, M_{fc}, P_{fc}, and Q_{fc} for the cracked tooth can refer to ref. [40].

It has been verified that the loaded tooth will not only induce the deformation of its own tooth, but also make the neighboring tooth generate the flexible deformation. In the double-tooth engagement region, the two engaged tooth pairs share one gear body, therefore, the double-tooth mesh stiffness will be considerably overestimated via the simple superposition of the single-tooth stiffness. Further, the coupling effect between the loaded neighboring teeth is proved to exert a considerable effect on the total mesh stiffness. Figure 4 shows the structural coupling effect between the loaded neighboring teeth of the healthy helical gear slice. It can be seen that the effective load-bearing regions for both engaged healthy teeth are S_f. However, the deflection angle will be formed between the center of the load-bearing and the geometric center with the presence of the crack fault. The effective load-bearing region S_f for the healthy helical gear slice and S_f' for the cracked helical gear slice are respectively shown in the Figure 5 with the bule and pink line. In addition, the analytical formulas of the coupling stiffness caused by the structural coupling effect for the healthy gear slice and the cracked gear slice are derived by Xie et al. [35] and Ning et al. [40], respectively. The stiffness K_{21} of the flexible deformation of the tooth #2 induced by the loaded tooth #1 and the stiffness K_{12} of the flexible deformation of the tooth #1 caused by the loaded tooth #2 for healthy and cracked helical gear slice can be expressed as [35,40]

$$\begin{aligned}
&\frac{1}{K_{21}} = \frac{\cos\alpha_1\cos\alpha_2}{Ed_w} \\
&\times\left[L_1\frac{u_1}{S_{f1}}\frac{u_2}{S_{f2}} + (M_1\tan\alpha_2 + P_1)\frac{u_1}{S_{f1}} + (Q_1\tan\alpha_1 + R_1)\right. \\
&\left.\times\frac{u_2}{S_{f1}} + (S_1\tan\alpha_1 + T_1)\tan\alpha_2 + U_1\tan\alpha_1 + V\right], \\
&\frac{1}{K_{12}} = \frac{\cos\alpha_1\cos\alpha_2}{Ed_w} \\
&\times\left[L_2\frac{u_1}{S_{f1}}\frac{u_2}{S_{f2}} + (M_2\tan\alpha_1 + P_2)\frac{u_2}{S_{f2}} + (Q_2\tan\alpha_2 + R_2)\right. \\
&\left.\times\frac{u_1}{S_{f2}} + (S_2\tan\alpha_2 + T_2)\tan\alpha_1 + U_2\tan\alpha_2 + V\right],
\end{aligned} \tag{16}$$

where the meaning of the variables can refer to Figures 4–5 for healthy and cracked helical gear slice, respectively. It is worth noting that the subscript 2 is replaced by 2c for the case of the crack fault. The calculation details of the coupling stiffness for the healthy helical gear slice can refer to ref. [35] while the cracked situation can refer to ref. [40].

2.3 Total mesh stiffness calculation for the cracked helical gear

Due to the presence of the helix angle, the engagement always begins at one end face and exists at the other one. Figure 6 shows the engaged process of the helical gear, the point A and B are the starting and ending points of the engagement, respectively. The contact line CD and GH are the transition region from the triple-tooth region to double-tooth region, and the contact line EF and IJ are the transition region from the double-tooth region to the triple-tooth region. ε_p denotes the total contact ratio and P_{bt} represents the pitch of the transverse. It is worth noting that although the contact ratio of helical gear is greater than 2, there is no situation that three teeth on the same gear slice engage simultaneously. Therefore, the structural coupling effect between neighbor-

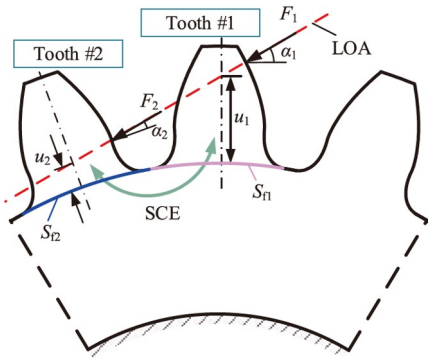

Figure 4 (Color online) Schematic of the structural coupling effect for the healthy helical gear slice.

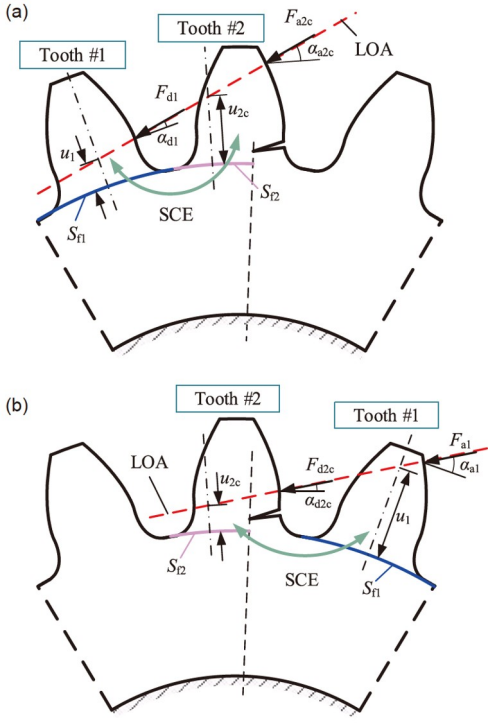

Figure 5 (Color online) Schematic of the structural coupling effect of the cracked helical gear slice. (a) Addendum region of the cracked tooth with dedendum region of the healthy tooth; (b) dedendum region of the cracked tooth with addendum region of the healthy tooth.

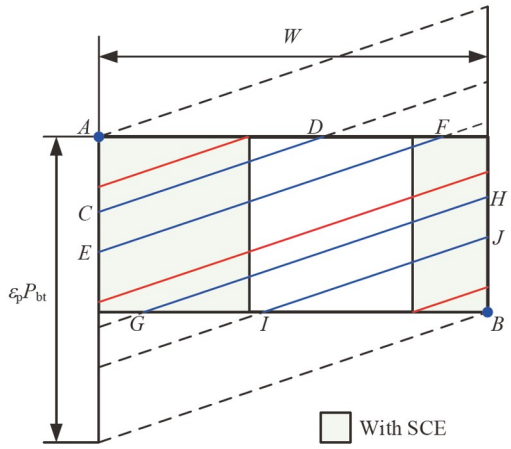

Figure 6 (Color online) Schematic of engaged process of helical gear.

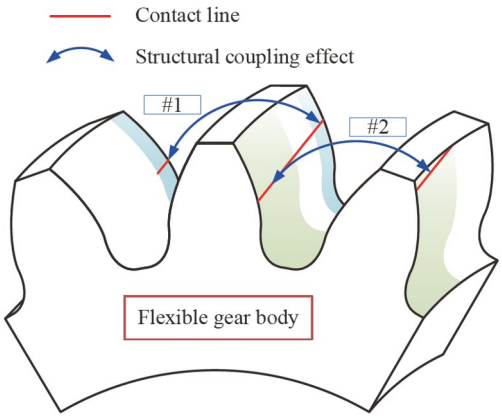

Figure 7 (Color online) Schematic of coupling effect between neighboring teeth for a helical gear.

ing teeth only exist in part of the helical gear slices.

To better display the coupling effect of the helical gear between the neighboring teeth, the three-dimensional schematic of the contact line for the engagement of the helical gear is shown in Figure 7. For the triple-tooth engagement, the effect of the elastic deformation between the neighboring teeth of the helical gear slice only exists in the shaded area and should be considered in the calculation of the total mesh stiffness for the cracked helical gear.

According to the equal principle of the total deformation of each slice along the line of action under the statical balanced status, the loaded static transmission error δ_L for each helical gear slice at one special mesh point are equal, which is the summation of the tooth deformation δ_t, gear-body induced deformation δ_f, contact deformation δ_h, deformation caused by structural coupling effect $\delta_{j,j+n}$, and tooth deviation e. The loaded static transmission error of jth helical gear slice can be expressed as the mathematical form as [37]

$$\delta_{Lj} = \delta_{tj} + \delta_{fj} + \delta_{hj} + \delta_{j,j+n} + e_j, \tag{17}$$

where the subscript n denotes the slice number.

When the helix angle in the helical gear pair is small, the contact ratio is low for this helical gear, of which the value is between 1 and 2. For the single-tooth engagement, there is no coupling deformation between the neighboring loaded teeth. Figure 8 shows the numbering diagram of the mesh point for different helical gear slice on the contact line, where the solid lines with green color denote the alternating area of the engaged teeth. Assuming that the mesh force acting on helical gear slice is F_j (j=1, 2, …, n), and the external torque acting on the driving gear is T_e, the summation of the mesh force on each helical slice is statically balanced with the external torque, namely

$$\sum_{j=1}^{n} F_j = \frac{T_e}{R_{bp}}, \tag{18}$$

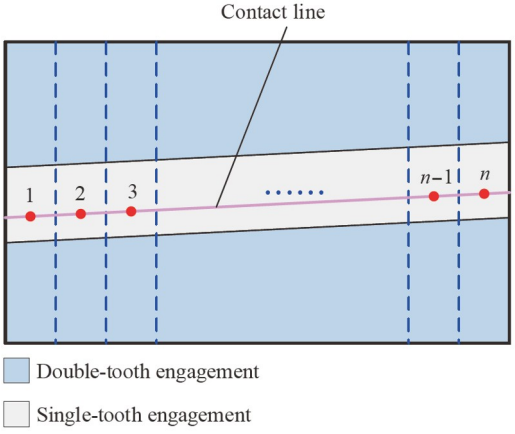

Figure 8 (Color online) Schematic of the helical gear slice numbering in single-tooth engagement.

where R_{bp} is the radius of the base circle for the driving gear.

Here, the summation of the stiffness components of tooth stiffness, contact stiffness, and gear body-induced stiffness is named as K_s, in which the linear contact stiffness is employed. It can be represented as

$$\frac{1}{K_s} = \frac{1}{K_{tp}} + \frac{1}{K_{tg}} + \frac{1}{K_{fp}} + \frac{1}{K_{fg}} + \frac{1}{K_h}, \tag{19}$$

where the subscripts p and g denote the driving and driven helical gear, respectively.

The relationship among the stiffness components, teeth deviations and the loads can be expressed as the following block matrix-vector form:

$$\begin{bmatrix} \mathbf{K}_1 & \mathbf{C}_1 \\ \mathbf{C}_2 & 0 \end{bmatrix} \mathbf{F}_L = \mathbf{E}_L, \tag{20}$$

where

$$\begin{aligned}
&\mathbf{K}_1 = \mathrm{diag}\left[\frac{1}{K_{\mathrm{s},1}} \quad \frac{1}{K_{\mathrm{s},2}} \quad \cdots \quad \frac{1}{K_{\mathrm{s},n}}\right]_{n\times n},\\
&\mathbf{C}_1 = [-1 \quad -1 \quad \cdots \quad -1]^{\mathrm{T}}_{n\times 1},\\
&\mathbf{C}_2 = [1 \quad 1 \quad \cdots \quad 1]_{1\times n},\\
&\mathbf{F}_{\mathrm{L}} = \left[F_1 \quad F_2 \quad \cdots \quad F_n \quad \delta_{\mathrm{L}}\right]^{\mathrm{T}}_{n\times 1},\\
&\mathbf{E}_{\mathrm{L}} = \left[-e_1 \quad -e_2 \quad \cdots \quad -e_n \quad \frac{T_{\mathrm{e}}}{R_{\mathrm{bp}}}\right]^{\mathrm{T}}_{n\times 1}.
\end{aligned} \tag{21}$$

Eq. (20) shows that there are n+1 unknown variables, namely F_1, F_2, …, F_n, δ_{L}, which can be only solved by the n+1 dimensional matrix. When the tooth contact loss occurs on the jth helical gear slice, the mesh force acting on it is nil, namely

$$F_j = 0, \quad \text{for } \delta_{\mathrm{L}} - e_j \leqslant 0. \tag{22}$$

Eq. (20) needs to remove the component of the tooth contact loss and then be solved again until the mesh force of all helical gear slice is greater than 0. The total mesh stiffness of the single-tooth engagement for the helical gear can be obtained by

$$K_{\mathrm{m}} = \frac{T_{\mathrm{e}}}{R_{\mathrm{bp}}\left[\delta_{\mathrm{L}} - \min(e_j)\right]}. \tag{23}$$

Figure 9 shows the numbering rules for the helical gear in the double-tooth engagement. It is worth noting that the helical gear slice without engagement is also numbered in order to better determine the engagement situation of each helical gear slices with the effect of tooth profile error. In addition, the coupling effect between the loaded neighboring teeth exists in the double-tooth engagement, which can be calculated by

$$\frac{1}{K_{j,j+n}} = \frac{1}{K_{\mathrm{p}j,j+n}} + \frac{1}{K_{\mathrm{g}j,j+n}}. \tag{24}$$

Therefore, the load distribution between the helical gear slices can be obtained by

$$\begin{bmatrix}
\mathbf{K}_1 & \mathbf{K}_{\mathrm{c}12} & \mathbf{C}_1\\
\mathbf{K}_{\mathrm{c}21} & \mathbf{K}_2 & \mathbf{C}_1\\
\mathbf{C}_2 & \mathbf{C}_2 & 0
\end{bmatrix}\mathbf{F}_{\mathrm{L}} = \mathbf{E}_{\mathrm{L}}, \tag{25}$$

where

$$\begin{aligned}
&\mathbf{K}_2 = \mathrm{diag}\left[\frac{1}{K_{\mathrm{s},n+1}} \quad \frac{1}{K_{\mathrm{s},n+2}} \quad \cdots \quad \frac{1}{K_{\mathrm{s},2n}}\right]_{n\times n},\\
&\mathbf{K}_{\mathrm{c}12} = \mathrm{diag}\left[\frac{1}{K_{1,n+1}} \quad \frac{1}{K_{2,n+2}} \quad \cdots \quad \frac{1}{K_{n,2n}}\right]_{n\times n},\\
&\mathbf{K}_{\mathrm{c}21} = \mathrm{diag}\left[\frac{1}{K_{n+1,1}} \quad \frac{1}{K_{n+2,2}} \quad \cdots \quad \frac{1}{K_{2n,n}}\right]_{n\times n},\\
&\mathbf{F}_{\mathrm{L}} = \left[F_1 \quad F_2 \quad \cdots \quad F_n \quad F_{n+1} \quad \cdots \quad F_{2n} \quad \delta_{\mathrm{L}}\right]^{\mathrm{T}}_{2n+1},\\
&\mathbf{E}_{\mathrm{L}} = \left[-e_1 \quad -e_2 \quad \cdots \quad -e_n \quad -e_{n+1} \quad \cdots \quad -e_{2n} \quad \frac{T_{\mathrm{e}}}{R_{\mathrm{bp}}}\right]^{\mathrm{T}}_{2n\times 1}.
\end{aligned} \tag{26}$$

Eq. (25) is a 2n+1 dimensional matrix equation which is equal to the numbers of the known variables (F_1, F_2, …, F_n, F_{n+1}, …, F_{2n}, δ_{L}). It is worth noting that the deformation component on the helical gear slice is zero if the contact line on this gear slice is out of the actual contact region. When the mesh forces of the solved helical gear slices are all greater than 0, eq. (23) can be employed to calculate the total mesh stiffness for the helical gear in the double-tooth engagement.

For the case of the slight larger helix angle, the contact ratio for the helical gear is between 2 and 3. The slice numbering for the helical gear in the triple-tooth engagement is displayed in Figure 10. There are 3n mesh points for the

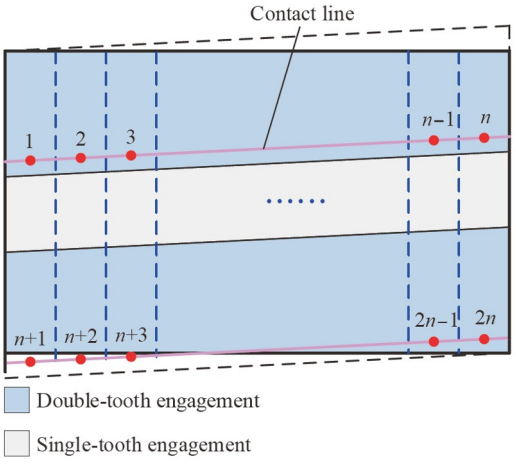

Figure 9 (Color online) Schematic of the helical gear slice numbering in double-tooth engagement.

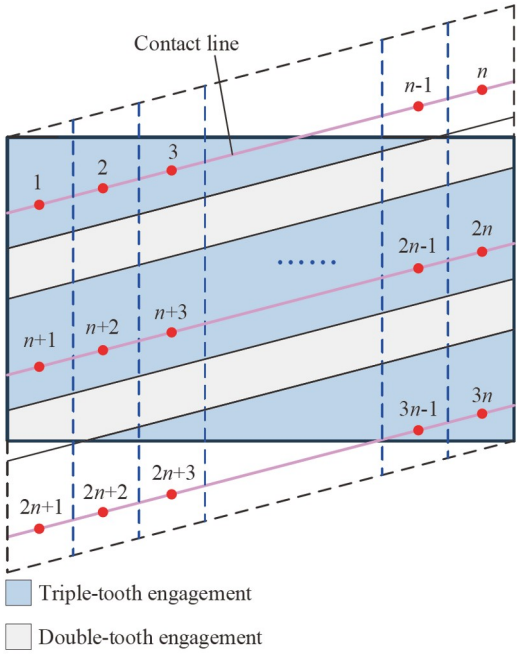

Figure 10 (Color online) Schematic of the helical gear slice numbering in triple-tooth engagement.

helical gear in the triple-tooth engagement, on which the mesh forces are assumed as $F_1, F_2, \ldots, F_n, F_{n+1}, \ldots, F_{2n}, F_{2n+1}, \ldots, F_{3n}$. The load distribution for the triple-tooth engagement can be calculated by

$$\begin{bmatrix} \mathbf{K}_1 & \mathbf{K}_{c12} & 0 & \mathbf{C}_1 \\ \mathbf{K}_{c21} & \mathbf{K}_2 & \mathbf{K}_{c23} & \mathbf{C}_1 \\ 0 & \mathbf{K}_{c32} & \mathbf{K}_3 & \mathbf{C}_1 \\ \mathbf{C}_2 & \mathbf{C}_2 & \mathbf{C}_2 & 0 \end{bmatrix} \mathbf{F}_L = \mathbf{E}_L, \tag{27}$$

where

$$\begin{aligned} \mathbf{K}_3 &= \mathrm{diag}\left[\frac{1}{K_{s,2n+1}} \quad \frac{1}{K_{s,2n+2}} \quad \cdots \quad \frac{1}{K_{s,3n}}\right]_{n\times n}, \\ \mathbf{K}_{c23} &= \mathrm{diag}\left[\frac{1}{K_{n+1,2n+1}} \quad \frac{1}{K_{n+2,2n+2}} \quad \cdots \quad \frac{1}{K_{2n,3n}}\right]_{n\times n}, \\ \mathbf{K}_{c32} &= \mathrm{diag}\left[\frac{1}{K_{2n+1,n+1}} \quad \frac{1}{K_{2n+2,n+2}} \quad \cdots \quad \frac{1}{K_{3n,2n}}\right]_{n\times n}, \\ \mathbf{F}_L &= \left[F_1 \quad F_2 \quad \cdots \quad F_n \quad F_{n+1} \quad \cdots \quad F_{2n} \quad F_{2n+1} \quad \cdots \quad F_{3n} \quad \delta_L\right]^{\mathrm{T}}_{3n+1}, \\ \mathbf{E}_L &= \\ &\left[-e_1 \; -e_2 \; \cdots \; -e_n \; -e_{n+1} \; \cdots \; -e_{2n} \; -e_{2n+1} \; \cdots \; -e_{3n} \; \frac{T_e}{R_{bp}}\right]^{\mathrm{T}}_{3n\times 1}. \end{aligned} \tag{28}$$

Through the iterative calculation, all load distribution results greater than 0 can be obtained. Similarly, eq. (23) can be employed to obtain the total mesh stiffness of the helical gear.

For the case of the higher contact ratio, it is not described in details here as they have the similar calculation equations. The above calculation process of the comprehensive stiffness can be summarized as the flow chart shown in Figure 11. The left module shows the traditional calculation method with purple color while the right module shows the improved calculation method with orange color.

3 Investigation on the crack fault effect on helical gear mesh stiffness

Based on the improved analytical model for the time-varying mesh stiffness calculation, the mesh stiffness results calculated by the improved model (Model #2) are compared with those by the finite element and traditional models (Model #1), where the traditional model is that the structural coupling effect is ignored. The effects of the different crack depths, crack propagation lengths, and helix angles on the time-varying mesh stiffness are investigated. The crack intersection is deemed as a constant value of 60°. The design parameters of the helical gear pair are listed in Table 1.

The mesh stiffness results calculated by the improved method are compared with those obtained by the finite element method to verify the correctness of the improved calculation method of the mesh stiffness for the helical gear pair. The crack fault parameters are consistent with those in ref. [34], reducing the errors as much as possible. The detailed settings of the parameters of the four types of the spatial crack are shown as follows:

Type-1: q_0=2.5 mm, q_{e2}=0 mm, L_{c2}=15 mm, l_0=3 mm, v=60°, β=10°;

Type-2: q_0=2.5 mm, q_{e1}=0.5 mm, L_{c1}=19 mm, l_0=3 mm, v=60°, β=10°;

Type-3: q_0=2.5 mm, q_{e2}=0 mm, L_{c2}=25 mm, l_0=2 mm, l_e=7 mm, v=60°, β=10°;

Type-4: q_0=2.5 mm, q_{e1}=2.5 mm, L_{c1}=30 mm, l_0=2 mm, l_e=7 mm, v=60°, β=10°;

where the details for the above variables are depicted in Figure 2.

Table 1 Design parameters of the helical gear pair

Parameters	Pinion	Gear
Normal module m_n (mm)	4	4
Normal pressure angle α_{n0} (°)	20	20
Number of teeth Z	40	40
Tooth width W (mm)	30	30
Addendum coefficient h_a^*	1	1
Tip clearance coefficient c^*	0.25	0.25
Young's modulus E (GPa)	212	212
Poisson's ratio υ	0.3	0.3
Radius of hub hole R_{int} (mm)	30	30
Torque T_e (N·m)	100	
Helix angle β (°)	10, 12, 14, 16, 18	

Figure 12 shows the time-varying mesh stiffness calculated by Model #1 and Model #2 compared with those obtained by the finite element model. It should be noted that the finite element results are extracted from ref. [34], where the detailed finite element model of the helical gear with spatial crack propagation was introduced. It can be clearly seen that the results from Model #2 match well with the finite element results for all the cases of the spatial crack propagation. For Model #1, the interactions between the loaded neighboring teeth induced by the flexible deformation of the gear body are ignored. When the multi-tooth engagement occurs, the engaged teeth share one gear body. The calculation method of the Model #1 is to obtain the comprehensive mesh stiffness by the simple superposition of the single tooth stiffness and ignoring the structural coupling effect, which would generate overestimated total mesh stiffness. The maximum relative error between the results of the mesh stiffness calculated by Model #1 and the finite element model is about 34%. When the coupling elastic effect between the loaded neighboring teeth is considered, the mesh stiffness amplitude is reduced in the multi-tooth engagement. The maximum relative errors of the mesh stiffness between Model #2 and

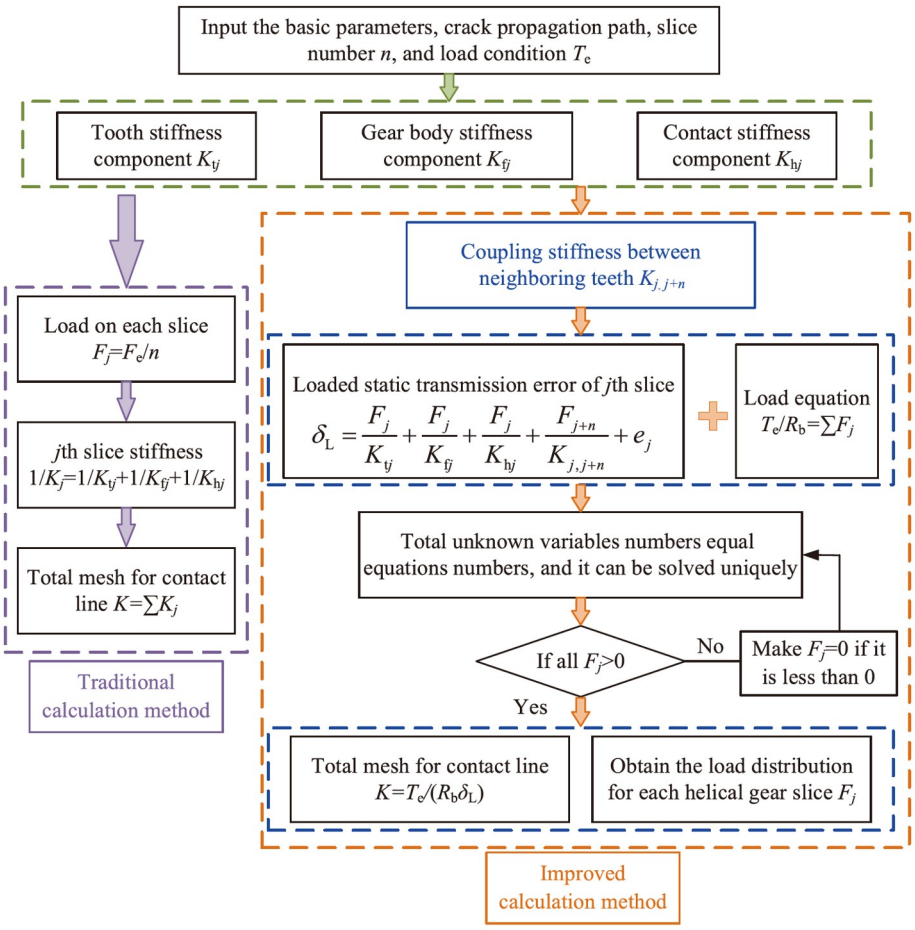

Figure 11 (Color online) Flowchart of the calculation process for the total mesh stiffness of the helical gear.

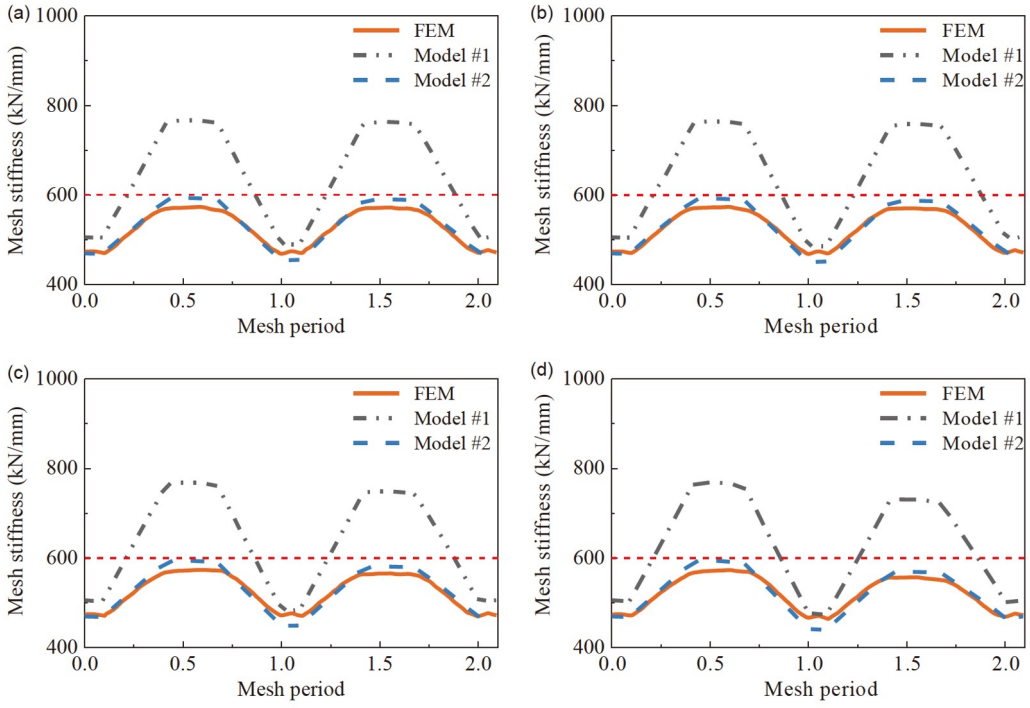

Figure 12 (Color online) Time-varying mesh stiffness obtained by different models and finite element model [34] with different crack types. (a) Type-1; (b) Type-2; (c) Type-3; (d) Type-4.

the finite element model for the double-tooth and the triple-tooth engagements are 4% and 6%, respectively. It is worth noting that the improved calculation method of the time-varying mesh stiffness catches better consistency with the finite element method compared with the traditional method. The improved stiffness calculation method can acquire more accurate mesh stiffness results. In addition, it is proved that the coupling effect of the elastic deformation between the loaded neighboring teeth should be considered in calculating the mesh stiffness. It is worth mentioning that the fault degree of the crack fault increases gradually from Type-1 to Type-4, and with the crack fault deterioration, the effective load bearing region will be reduced for both the tooth part and gear body. Thus, the total mesh stiffness will also present a decreasing trend. A reference line with dashed line in red color is draw at the mesh stiffness of 600 kN/mm to improve the readability of this paper. There are no apparent differences in the four result curves for the first multi-tooth engagement, while the obvious variations can be found in the second multi -tooth engagement. This reason may be that the differences of the crack fault mainly are reflected in the addendum region, while there are no obvious differences in the dedendum region for the four crack types. The addendum crack effect on the mesh stiffness calculation is not included in the first multi-tooth engagement while that can be reflected in the second one. Therefore, there are different variations in the two multi-tooth engagements for the four crack types. However, there are still minor errors between the theoretical calculation and finite element results may be induced by neglecting of the coupling effect between the neighboring slices and assuming that the parameters during the meshing process are constant. Establishing a more refined model and considering more influencing factors is necessary to carry out the relevant research to improve the calculation accuracy.

As an essential design parameter of the helical gear, the helix angle value will exert a considerable effect on the mesh behaviors of the helical gear systems. Figure 13(a) depicts the effect of the different helix angles on the mesh stiffness calculated by the improved model (Model #2) while Figure 13(b) shows the results calculated by the traditional model (Model #1). The crack fault parameters are q_0=3 mm, q_{e1}=2 mm, L_{c1}=30 mm, l_0=2 mm, l_e=7 mm, v=60°. The triple-tooth engagement region is drawn with the shadow to improve the readability, and the rest region in one mesh period is the double-tooth engagement. The shadow region with green color is the triple-tooth engagement region with the helix angle of 12°. With the helix angle increment, the triple-tooth engagement region presents the growth on the basis of the region with the helix angle of 12°, and the additional regions are shadowed with the corresponding colors for different helix angles. However, the corresponding double-tooth engagement shows a decline with the helix angle increment in

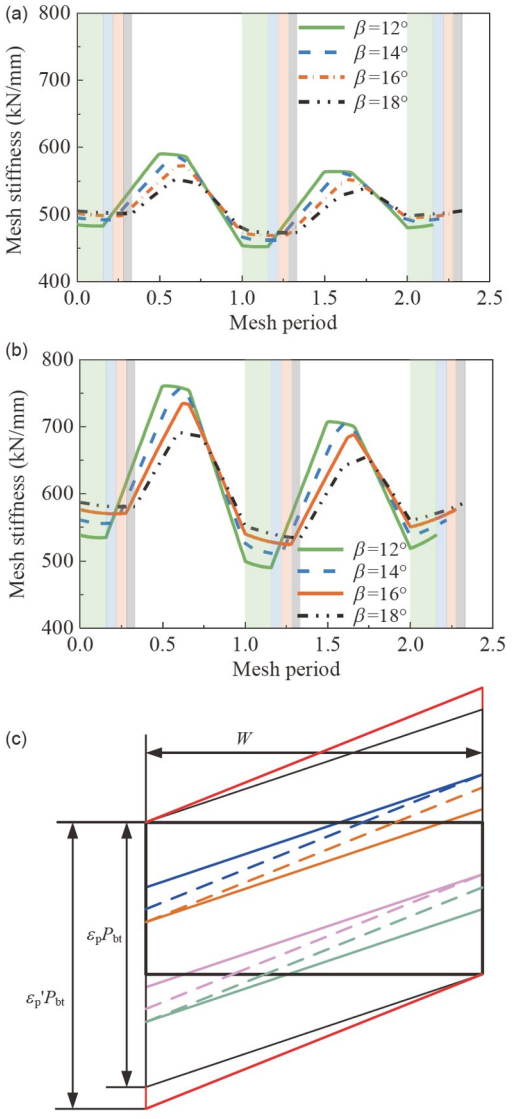

Figure 13 (Color online) Effect of different helix angle on the mesh behaviors. (a) Mesh stiffness obtained by Model #2; (b) mesh stiffness obtained by Model #1; (c) contact line.

one engagement period. It can be seen that the alternate process between the triple-tooth and double-tooth engagement become moderated with the helix angle growth, and the difference value of the mesh stiffness amplitude between the triple-tooth and double-tooth engagements decline. As the helix angle rises from 12° to 18°, the total contact ratio grows from 2.157 to 2.333, which means that the mesh period proportion of the triple-tooth engagement experiences a considerable rise while that of the double-tooth engagement drops in the meshing process. It can be seen that both the amplitude and variation of the mesh stiffness calculated by the improved model are decreased, as shown in Figure 13(a), compared with the results obtained from the traditional model which are shown in Figure 13(b). The stiffness of both tooth and gear body are reduced due to the reduction of the effective load bearing region with the crack faults. The mesh

stiffness fluctuations are alleviated because there are fewer deformations induced by the structural coupling effect when the crack tooth engages in its dedendum region than that meshes in its addendum region, which has been demonstrated in ref. [40]. Therefore, the improved model for calculating the mesh stiffness with crack faults has higher accuracy than the traditional model. Figure 13(c) shows the contact line of the helical pair with different helix angles, where the colored lines denote the alternating boundary of the engaged teeth. The solid line represents the minor helix angle while the dashed line denotes the major helix angle. It is worth noting that the helix angle increment leads to contact line increase in the triple-tooth engagement and the decrease of that in the double-tooth engagement. In addition, the mesh stiffness amplitude variations present a nonlinear relationship with the helix angle increment. The relative stiffness amplitude growth is in the range of 2%–4% for the triple-tooth engagement while the relative reduction of that is in the range of 0.8%–6.4% for the double-tooth engagement. As the cracked helical gear meshed from the dedendum region to the addendum region, the stiffness amplitudes in the dedendum region are larger than those in the addendum region.

The mesh stiffness of the cracked helical gear pair with different depths of the spatial crack propagation is displayed in Figure 14, namely (1) q_0=1 mm, q_e=0 mm, (2) q_0=2 mm, q_e=1 mm, (3) q_0=3 mm, q_e=2 mm, and (4) q_0=4 mm, q_e=3 mm. The mesh stiffness results can reflect the alternating process between the triple- and double-tooth engagements.

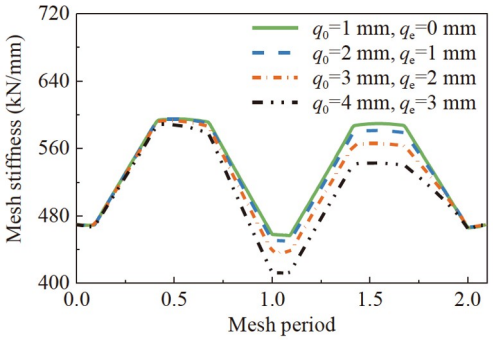

Figure 14 (Color online) Effect of different crack depth on the mesh stiffness.

Due to the presence of the helix angle, the contact line experiences the process of a moderate increase, followed by a steady decrease. Here the other parameters of the crack fault are L_{c1}=30 mm, l_0=2 mm, l_e=7 mm, v=60°, β=10°. The dramatic decline can be found in this figure when the spatial crack propagation is introduced in the stiffness calculation model. The mesh stiffness reduction presents a nonlinear relationship with the growth of the depth of the spatial crack propagation. It is worth noting that the mesh stiffness is sensitive to the crack propagation, and the amplitudes of the mesh stiffness present the nonlinear drops when the crack faults propagated with a constant degree.

The load distributions of the cracked tooth with different propagation depths are shown in Figure 15. It is worth noting

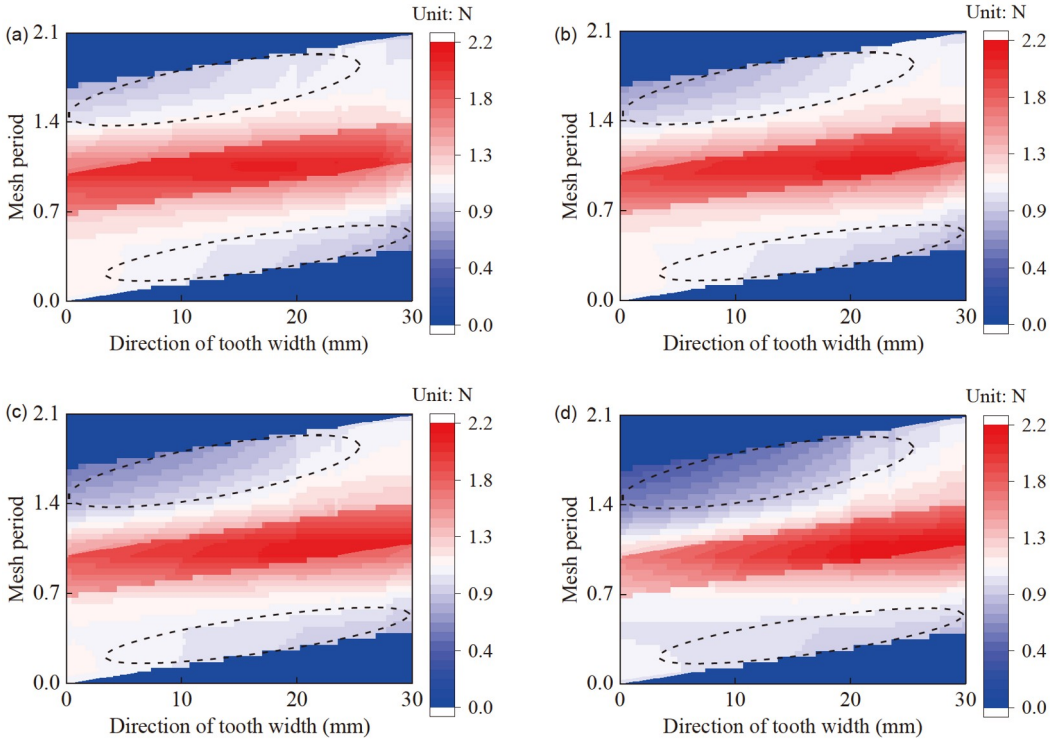

Figure 15 (Color online) Load distribution of the cracked tooth with different crack depth. (a) q_0=1 mm, q_e=0 mm; (b) q_0=2 mm, q_e=1 mm; (c) q_0=3 mm, q_e=2 mm; (d) q_0=4 mm, q_e=3 mm.

that the crack propagates from the origin of the coordinates along the tooth width direction. When the size of the crack fault is small, the differences in the load distribution along the tooth width direction is not obvious, such as Figure 15(a) and 15(b). In the contour figure, the warm colors correspond to larger values, and cool colors correspond to smaller ones. With the crack depth rise, the differences in the load distribution along the contact line are gradually observed, such as the region circled by the dashed line shown Figure 15(c) and 15(d). The specific mesh point on the contact line will be assigned the lower loads when the crack faults is more serious. The region with more serious crack depth propagation has less load distribution while the load distribution at the other end of the tooth width is larger.

The case parameters for the crack fault are q_0=3 mm, q_{e1}=3 mm, l_0=2 mm, l_e=7 mm, v=60°, β=10°. The variations of the mesh stiffness versus the propagation length of the spatial crack are shown in Figure 16. The equally obvious variations can be observed in the alternating boundary between the triple- and double-tooth engagements. In addition, the same phenomenon of the variation laws of the mesh stiffness could be seen for the crack length and depth propagations.

Here, the load distributions of the cracked tooth are investigated under the same crack depth and different propagation lengths, which are demonstrated in Figure 17. With the crack length propagation from L_c/W=25% to 100% with the interval of 25%, and the corresponding coordinates along the tooth width are 7.5, 15, 22.5, and 30 mm, the discrepancies of the load distribution along the tooth width firstly increase and then decrease. It can be seen from Figure 17(a)–(c) that the load distribution on the left zone is obviously smaller than that on the right zone with the crack propagation. A similar phenomenon can be found in the variation of crack length propagation when it is shown in the contour figure with the crack depth propagation. With the penetrative end face crack with the same crack depth, the left part of the load distributions is still less than the right part shown in Figure 17(d), indicating that the crack occurring at the root region will exert a stronger effect on the mesh stiffness as the meshing process from the crack location to the tip region will be affected.

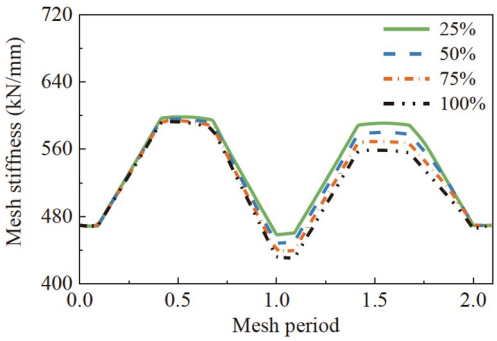

Figure 16 (Color online) Effect of different crack propagation length on the mesh stiffness.

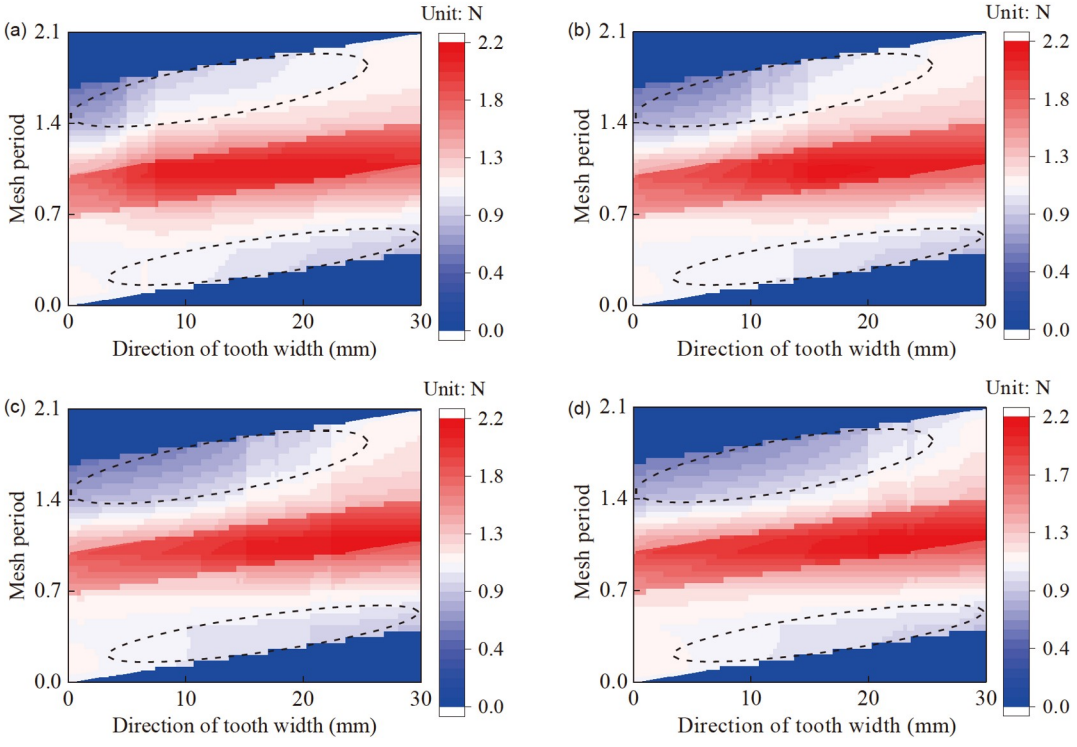

Figure 17 (Color online) Load distribution of the cracked tooth with different crack length. (a) L_c/W=25%; (b) L_c/W=50%; (c) L_c/W=75%; (d) L_c/W=100%.

4 Conclusions

In this study, the analytical mesh stiffness calculation method is improved for the helical gear pair with the spatial crack propagation considering the effective load-bearing region of the gear body with the crack fault in the calculations of the gear body-induced stiffness and the flexible coupling stiffness between the neighboring teeth. The action mechanism of the structural coupling effect in the helical gear pair is revealed analytically based on the static balance principle, namely the loaded static transmission errors are consistent for all the engaged helical gear slices.

Compared with the traditional method, the mesh stiffness calculated using the improved method are compared with the finite element results, which demonstrate a better consistency. With the helix angle increment from 12° to 18°, there are the mesh stiffness growth in the triple-tooth engagement while an opposite phenomenon occurs in the double-tooth engagement. Both the amplitude and the variation of the mesh stiffness decline due to the consideration of the coupling effect between the neighboring teeth with the crack faults. Besides, with the variations of the crack propagation size in depth or length, the region with a more serious crack fault has the less load distribution. The mesh stiffness reduction presents a nonlinear relationship with the growth of the depth and length of the spatial crack propagation. This improved method is capable of catching the accurate results of the total mesh stiffness and the load distribution for the further dynamic analysis of the helical gear.

It is worth noting that such a coupling effect between the neighboring loaded tooth pairs is also suitable for situations with other different fault types, such as wear, spalling, and tooth-broken faults. The proposed model has the property that the fault action mechanism can be reflected through the stiffness or displacement excitation for different fault types.

This work was supported by the National Natural Science Foundation of China (Grant Nos. 52022083, 52275132 and 51735012).

1 Tang X, Chen J, Liu T, et al. Distributed deep reinforcement learning-based energy and emission management strategy for hybrid electric vehicles. IEEE Trans Veh Technol, 2021, 70: 9922–9934
2 Wang Q, Xiao Z, Zhou J, et al. A dynamic detection method for polygonal wear of railway wheel based on parametric power spectral estimation. Vehicle Syst Dyn, 2022, doi: 10.1080/00423114.2022.2117058
3 Lewicki D G, Ballarini R. Effect of rim thickness on gear crack propagation path. J Mech Des, 1997, 119: 88–95
4 Verma J G, Kumar S, Kankar P K. Crack growth modeling in spur gear tooth and its effect on mesh stiffness using extended finite element method. Eng Fail Anal, 2018, 94: 109–120
5 Wang Q, Chen K, Zhao B, et al. An analytical-finite-element method for calculating mesh stiffness of spur gear pairs with complicated foundation and crack. Eng Fail Anal, 2018, 94: 339–353
6 Chen K, Huangfu Y, Ma H, et al. Calculation of mesh stiffness of spur gears considering complex foundation types and crack propagation paths. Mech Syst Signal Processing, 2019, 130: 273–292
7 Raghuwanshi N K, Parey A. Experimental measurement of gear mesh stiffness of cracked spur gear by strain gauge technique. Measurement, 2016, 86: 266–275
8 Patel A, Shakya P. Spur gear crack modelling and analysis under variable speed conditions using variational mode decomposition. Mechanism Machine Theor, 2021, 164: 104357
9 Chen Z, Shao Y. Dynamic simulation of spur gear with tooth root crack propagating along tooth width and crack depth. Eng Fail Anal, 2011, 18: 2149–2164
10 Chen Z, Shao Y. Mesh stiffness calculation of a spur gear pair with tooth profile modification and tooth root crack. Mechanism Machine Theor, 2013, 62: 63–74
11 Mohammed O D, Rantatalo M, Aidanpää J O. Improving mesh stiffness calculation of cracked gears for the purpose of vibration-based fault analysis. Eng Fail Anal, 2013, 34: 235–251
12 Wan Z, Cao H, Zi Y, et al. An improved time-varying mesh stiffness algorithm and dynamic modeling of gear-rotor system with tooth root crack. Eng Fail Anal, 2014, 42: 157–177
13 Ma H, Song R, Pang X, et al. Time-varying mesh stiffness calculation of cracked spur gears. Eng Fail Anal, 2014, 44: 179–194
14 Ma H, Pang X, Feng R, et al. Fault features analysis of cracked gear considering the effects of the extended tooth contact. Eng Fail Anal, 2015, 48: 105–120
15 Ma H, Pang X, Zeng J, et al. Effects of gear crack propagation paths on vibration responses of the perforated gear system. Mech Syst Signal Processing, 2015, 62-63: 113–128
16 Pandya Y, Parey A. Simulation of crack propagation in spur gear tooth for different gear parameter and its influence on mesh stiffness. Eng Fail Anal, 2013, 30: 124–137
17 Pandya Y, Parey A. Crack behavior in a high contact ratio spur gear tooth and its effect on mesh stiffness. Eng Fail Anal, 2013, 34: 69–78
18 Yu W, Shao Y, Mechefske C K. The effects of spur gear tooth spatial crack propagation on gear mesh stiffness. Eng Fail Anal, 2015, 54: 103–119
19 Cui L, Huang J, Zhai H, et al. Research on the meshing stiffness and vibration response of fault gears under an angle-changing crack based on the universal equation of gear profile. Mechanism Machine Theor, 2016, 105: 554–567
20 Meng Z, Shi G, Wang F. Vibration response and fault characteristics analysis of gear based on time-varying mesh stiffness. Mechanism Machine Theor, 2020, 148: 103786
21 Jiang H, Liu F. Mesh stiffness modelling and dynamic simulation of helical gears with tooth crack propagation. Meccanica, 2020, 55: 1215–1236
22 Tang X, Zou L, Yang W, et al. Novel mathematical modelling methods of comprehensive mesh stiffness for spur and helical gears. Appl Math Model, 2018, 64: 524–540
23 Huangfu Y, Chen K, Ma H, et al. Meshing and dynamic characteristics analysis of spalled gear systems: A theoretical and experimental study. Mech Syst Signal Processing, 2020, 139: 106640
24 Huangfu Y F, Chen K K, Ma H, et al. Investigation on meshing and dynamic characteristics of spur gears with tip relief under wear fault. Sci China Technol Sci, 2019, 62: 1948–1960
25 Chen Z, Zhang J, Zhai W, et al. Improved analytical methods for calculation of gear tooth fillet-foundation stiffness with tooth root crack. Eng Fail Anal, 2017, 82: 72–81
26 Jiang J, Chen Z, Zhai W, et al. Vibration characteristics of railway locomotive induced by gear tooth root crack fault under transient conditions. Eng Fail Anal, 2020, 108: 104285
27 Chen Z, Zhai W, Wang K. Vibration feature evolution of locomotive with tooth root crack propagation of gear transmission system. Mech Syst Signal Processing, 2019, 115: 29–44
28 Ning J, Chen Z, Wang Y, et al. Vibration feature of spur gear transmission with non-uniform depth distribution of tooth root crack along tooth width. Eng Fail Anal, 2021, 129: 105713
29 Yang L, Wang L, Shao Y, et al. A new calculation method for tooth fillet foundation stiffness of cracked spur gears. Eng Fail Anal, 2021,

121: 105173
30 Yang L, Wang L, Yu W, et al. Investigation of tooth crack opening state on time varying meshing stiffness and dynamic response of spur gear pair. Eng Fail Anal, 2021, 121: 105181
31 Wang S, Zhu R. An improved mesh stiffness calculation model for cracked helical gear pair with spatial crack propagation path. Mech Syst Signal Processing, 2022, 172: 108989
32 Feng M, Ma H, Li Z, et al. An improved analytical method for calculating time-varying mesh stiffness of helical gears. Meccanica, 2018, 53: 1131–1145
33 Ma H, Zeng J, Feng R, et al. An improved analytical method for mesh stiffness calculation of spur gears with tip relief. Mechanism Machine Theor, 2016, 98: 64–80
34 Huangfu Y, Chen K, Ma H, et al. Deformation and meshing stiffness analysis of cracked helical gear pairs. Eng Fail Anal, 2019, 95: 30–46
35 Xie C, Hua L, Han X, et al. Analytical formulas for gear body-induced tooth deflections of spur gears considering structure coupling effect. Int J Mech Sci, 2018, 148: 174–190
36 Xie C, Shu X. A new mesh stiffness model for modified spur gears with coupling tooth and body flexibility effects. Appl Math Model, 2021, 91: 1194–1210
37 Chen Z, Zhou Z, Zhai W, et al. Improved analytical calculation model of spur gear mesh excitations with tooth profile deviations. Mechanism Machine Theor, 2020, 149: 103838
38 Chen Z, Ning J, Wang K, et al. An improved dynamic model of spur gear transmission considering coupling effect between gear neighboring teeth. NOnlinear Dyn, 2021, 106: 339–357
39 Chen Z G, Zhi Y S, Ning J Y. Study on the effect of tooth root crack on gear body stiffness and coupling stiffness between adjacent teeth (in Chinese). J Mechanical Transmission, 2022, 46: 1–8
40 Ning J, Chen Z, Zhi Y, et al. Improved analytical method for gear body-induced deflections with tooth root crack considering structural coupling effect. Eng Fail Anal, 2022, 137: 106400
41 Asi O. Fatigue failure of a helical gear in a gearbox. Eng Fail Anal, 2006, 13: 1116–1125
42 Amiri Rad A, Forouzan M R, Sadeghi Dolatabadi A. Three-dimensional fatigue crack growth modelling in a helical gear using extended finite element method. Fatigue Fract Engng Mater Struct, 2014, 37: 581–591
43 Ajmi M, Velex P. A model for simulating the quasi-static and dynamic behaviour of solid wide-faced spur and helical gears. Mechanism Machine Theor, 2005, 40: 173–190
44 Wang Q, Zhao B, Fu Y, et al. An improved time-varying mesh stiffness model for helical gear pairs considering axial mesh force component. Mech Syst Signal Processing, 2018, 106: 413–429
45 Sainsot P, Velex P, Duverger O. Contribution of gear body to tooth deflections—A new bidimensional analytical formula. J Mech Des, 2004, 126: 748–752